STRUCTURAL BIOLOGY

Formation of cellular close-ended tunneling nanotubes through mechanical deformation

Minhyeok Chang[1]†‡, O-chul Lee[1]†, Gayun Bu[1]†, Jaeho Oh[1], Na-Oh Yunn[2], Sung Ho Ryu[3], Hyung-Bae Kwon[4], Anatoly B. Kolomeisky[5], Sang-Hee Shim[6], Junsang Doh[7], Jae-Hyung Jeon[1,8]*, Jong-Bong Lee[1,8,9]*

Membrane nanotubes or tunneling nanotubes (TNTs) that connect cells have been recognized as a previously unidentified pathway for intercellular transport between distant cells. However, it is unknown how this delicate structure, which extends over tens of micrometers and remains robust for hours, is formed. Here, we found that a TNT develops from a double filopodial bridge (DFB) created by the physical contact of two filopodia through helical deformation of the DFB. The transition of a DFB to a close-ended TNT is most likely triggered by disruption of the adhesion of two filopodia by mechanical energy accumulated in a twisted DFB when one of the DFB ends is firmly attached through intercellular cadherin-cadherin interactions. These studies pinpoint the mechanistic questions about TNTs and elucidate a formation mechanism.

INTRODUCTION

As an intercellular communication, tunneling nanotubes (TNTs) or membrane nanotubes are submicrometer thin routes that directly connect distant cells (*1*). TNTs mainly originate from plasma membrane protrusions containing filamentous actins (F-actins) (*1*), but microtubule- or cytokeratin filament–associated TNTs have also been found (*2*, *3*). Organelles (*1*), vesicles (*4*), viruses (*5*), morphogens (*6*), RNAs (*7*, *8*), and receptors (*9*) can be transported through this unique structure in various types of cells, including neuronal (*1*), immune (*4*), cancerous (*7*, *10*), epithelial (*11*), and stem cells (*6*), as well as in *Drosophila* tissue (*9*, *12*). Moreover, a recent study on primary cancer cells showed the pathological importance of TNT formation in tumor metastasis (*7*). Thus, TNTs may play an important role in long-distance communication between cells for human disease and development.

Imaging studies on cultured cells suggested that TNTs can initially form from thin finger-like actin assembly-driven protrusions (filopodia) or direct contact between cell bodies (*13*). The resulting TNTs are suspended between the cells (*1*), maintaining an intercellular distance up to ~500 times longer than the thickness of the TNT (hundreds of nanometers). However, the formation mechanism is poorly understood: How do short and dynamic filopodia form long and stable TNTs, and what triggers the transformation of the filopodia into TNT? There is also a highly controversial question about whether a TNT is open-ended or close-ended in vivo (*14*). The answer to this question provides vital clues as to how intercellular materials can be transferred from one cell to another.

We visualized the formation processes of F-actin–based TNTs using real-time fluorescence microscopy and super-resolution fluorescence microscopy. Here, a single filopodial bridge (SFB) connecting distinct cells is termed as a TNT. Filopodia exhibit various physical features, such as growth, retraction, bending, rotation, and helical buckling (*15*), due to F-actin dynamics. The random motion of filopodia results in transient contact. The intercellular interactions of cell adhesion molecules on the filopodia maintain a double filopodial bridge (DFB) connecting cells. Notably, our super-resolution fluorescent imaging shows that a helically deformed DFB is eventually transformed into a TNT. The end of the TNT is tightly linked to the paired cell body through intercellular interactions of cadherin cell adhesion molecules, through which Ca^{2+} ions can be transferred unidirectionally. These observations strongly suggest a close-ended TNT. We developed a physical model of TNT formation via helical deformation of DFB, which was validated by measuring their elastic characteristics and computer-assisted simulations. These studies reveal the mechanism of TNT formation, along with information on a unique nanostructure of the DFB that plays a critical role in forming long-standing TNTs connecting cells.

RESULTS

The transition of a DFB into an SFB

To visualize the dynamics of the formation of actin-based SFBs in cells, we tagged cellular actin filaments (F-actin) with an actin-binding 17–amino acid peptide (Lifeact) that was genetically engineered to contain enhanced green fluorescent protein (EGFP) (green) or mCherry (red) (Fig. 1A and Methods) (*16*), which were imaged using line scan confocal microscopy (LSCM) (*17*). To image DFBs or SFBs suspended in the medium, we scanned along the *z* direction from the surface of the imaging dish. The colocalization images illustrate the two-color filopodial bridges (FBs) formed by two filopodia protruding from different cells (DFBs; Fig. 1A) or single-color FBs between cells (SFBs; Fig. 1A). We confirmed by plasma membrane imaging that a DFB was not a single membrane tube formed by the fusion of two filopodia but a bridge consisting of two isolated

[1]Department of Physics, Pohang University of Science and Technology (POSTECH), Pohang 37673, Korea. [2]POSTECH Biotech Center, Pohang 37673, Korea. [3]Department of Life Sciences, POSTECH, Pohang 37673, Korea. [4]Department of Neuroscience, Johns Hopkins University School of Medicine, Baltimore, MD 21205, USA. [5]Department of Chemistry, Rice University, Houston, TX 77005, USA. [6]Department of Chemistry, Korea University, Seoul 02481, Korea. [7]Department of Materials Science and Engineering, Seoul National University, Seoul 08826, Korea. [8]Asia Pacific Center for Theoretical Physics (APCTP), Pohang 37673, Korea. [9]School of Interdisciplinary Bioscience and Bioengineering, POSTECH, Pohang 37673, Korea.
*Corresponding author. Email: jblee@postech.ac.kr (J.-B.L.); jeonjh@postech.ac.kr (J.-H.J.)
†These authors contributed equally to this work.
‡Present address: Department of Neuroscience, Johns Hopkins University School of Medicine, Baltimore, MD 21205, USA.

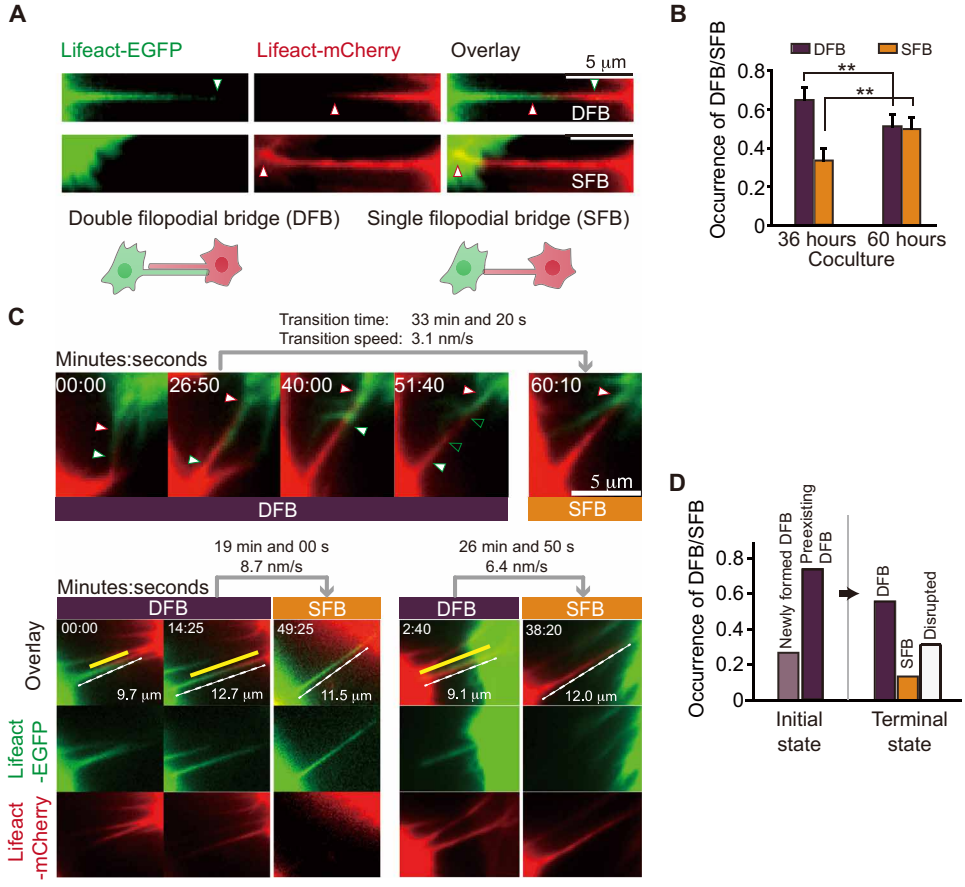

Fig. 1. SFB formation from DFB. (**A**) Colocalization of F-actin in each HeLa cell transfected to contain Lifeact-EGFP or Lifeact-mCherry in each HeLa cell. The HeLa cells were cultured together in a 1:1 ratio (Methods). The triangles indicate the end of each actin protrusion (filopodium) that consists of intercellular connections. (**B**) Frequencies of DFBs and SFBs in cells fixed at different times showing a significant increase in the frequency of SFBs from 33 to 50% ($n = 242$ and 158 SFBs obtained from $N_{cell} = 116$ and 60 cell pairs in $N_{exp} = 4$ independent experiments). The $P = 0.008$ (DFB) and $P = 0.010$ (SFB) by two-sided Student's t test (degrees of freedom = 6 , ** for $P \leq 0.01$). The error bars indicate the SD. (**C**) Dynamics of the transition of DFBs to SFBs during real-time imaging of live HeLa cells. Yellow lines indicate the overlap of two filopodia. (**D**) During a 1-hour-long time-lapse imaging, some newly formed ($n = 11$) or preexisting ($n = 33$) DFBs developed into new SFBs ($n = 6$, 13%) or were disrupted ($n = 14$, 31%), while others remained in the DFB states ($n = 25$, 56%). The number of cells $N_{cell} = 17$ and time-lapse experiments were performed by recording every 5 or 10 s with a 100-ms exposure time.

filopodia (fig. S1). As the coculture time increased from 36 to 60 hours, the occurrence of SFBs also increased significantly from 33 ± 6% to 50 ± 6%. DFBs and SFBs extended from 8.7 ± 3.8 μm to 10.5 ± 6.1 μm and 8.1 ± 3.5 μm to 9.1 ± 4.5 μm, respectively (Fig. 1B). On average, two suspended filopodial bridges (DFB and SFB) per cell pair were observed between 36 and 60 hours after coculture.

Real-time tracking of actin-based membrane protrusions revealed the initial and intermediate states of SFB formation (Fig. 1C). Physical contact between fluctuating filopodia protruding from green and red cells formed DFBs (Fig. 1C, top and movies S1 and S2, 00:00, minutes:seconds); the resulting DFBs appeared to extend until one or both filopodia reached the other cell body (movie S2, 26:40), at which time one filopodium was then released from the other filopodium and retracted back to the cell body and a single filopodium remained connected between the two cells to form SFB lastly (movie S2, 39:40 to 60:10). When we looked at six transitions of DFB to SFB, the transition time was at least 25 ± 13 min, and the transition rate was 6.0 ± 3.3 nm/s. The contact and dislodgement of lamellipodia from two cells also initiated DFB formation (fig. S2A and movie S3). These results suggest that DFBs develop into SFBs when one filopodium is released from the other and then retracts back to its cell body (Fig. 1C, fig. S2B, and movie S3) in time-lapse imaging for 1 hour after at least 36 hours of coculture. Highly dynamic F-actin motion is likely to enhance the physical contact of filopodia for DFB formation. The breakage of DFBs, which results in two separate filopodia, was often observed due to large fluctuations of the filopodia (31%; Fig. 1D and movie S1). This may imply that the strong binding of two filopodia is necessary to form a stable intermediate state of the DFB.

Intercellular N-cadherin interaction connects an SFB to its partner cell

The binding of the extracellular domains of cadherin molecules for cell-to-cell adhesion is a promising potential mechanism of DFB formation and stabilization (*18*). We confirmed the presence of N-cadherin molecules on DFBs or SFBs in our previous report (*19*). As we expected, the occurrence of DFBs or SFBs (DFBs/SFBs) per cell decreased by ~50% in HeLa cells when endogenous N-cadherin, a classical adhesion protein expressed in HeLa cells, was down-regulated by small interfering RNA (siRNA) (Fig. 2A and fig. S3). We also carried out a Ca^{2+} depletion experiment to interrupt the

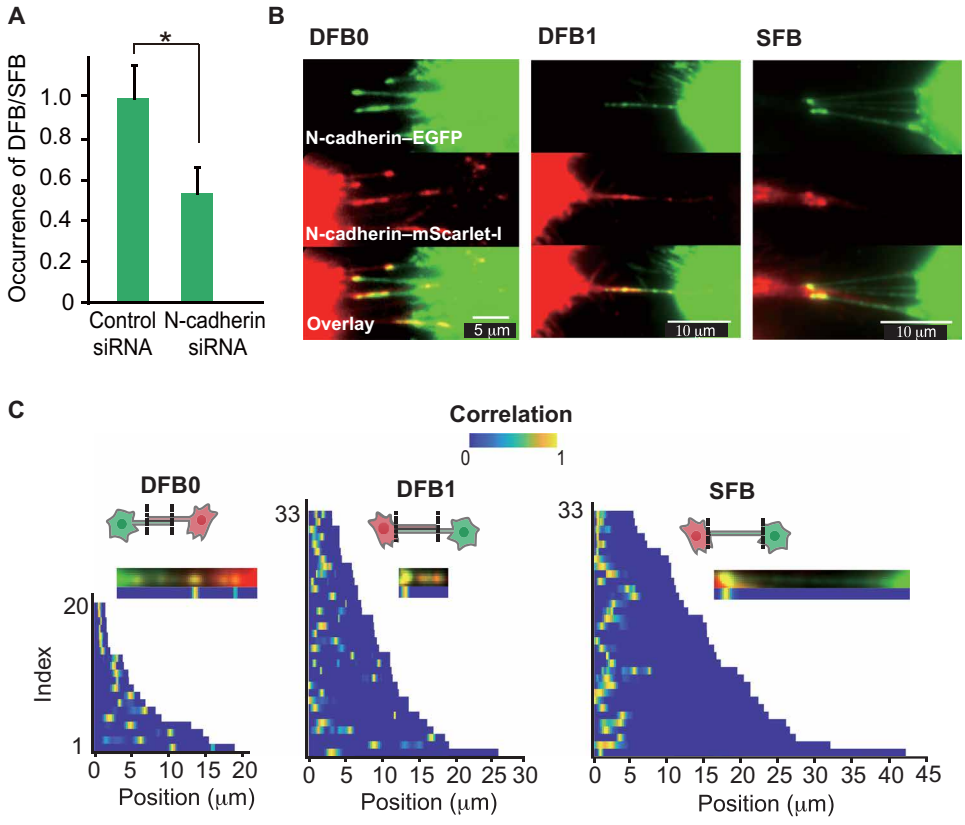

Fig. 2. N-cadherin clusters on DFBs/TNTs. (**A**) DFB or SFB occurrence in N-cadherin down-regulated cells 72 hours after 60 nM siRNA transfection ($n = 222$, $N_{cell} = 538$ for control RNA and $n = 147$, $N_{cell} = 741$ for siRNA, normalized by control). *$P = 0.019$ by one-sided Student's t test. (**B**) N-cadherin molecules on DFBs and SFBs colocalized in live HeLa cells expressing N-cadherin–EGFP or N-cadherin–mScarlet-I. The images were obtained by averaging the intensity of each pixel in 91 consecutive frames. (**C**) Local correlation between EGFP and mScarlet-I labeled on N-cadherin in two-color imaging (Methods). The local correlations were normalized with the maximum local correlation of each DFB or SFB, and the negative local correlation was set to 0.

interaction between the extracellular domains of N-cadherin molecules (*20*). The frequency of filopodial separation in DFBs and dissociation of SFBs from the paired cell were significantly enhanced after Ca^{2+} depletion by the treatment of EGTA (fig. S4). Together, these results provide substantial evidence that the formation of a DFB results from the dimerization of N-cadherin extracellular domains from two different filopodia.

To visualize N-cadherin molecules in the DFBs or SFBs of living cells, we cocultured and imaged HeLa cells expressing N-cadherin molecules fused with EGFP (green) and mScarlet-I (red), respectively (Fig. 2B). N-cadherin clusters were randomly distributed along DFBs or localized only on the junctions of the filopodium's end and cell bodies (DFB0, DFB1, and SFB; Fig. 2B). The number after DFB (DFB0, DFB1, and DFB2) denotes the number of junction(s) between the filopodium's end and the paired cell body (Fig. 2, B and C). DFB2, with two connections, was rarely observed (fig. S5). The degree of N-cadherin accumulation between two cells was defined as the local correlation coefficient at each pixel (Methods and Fig. 2B, overlay), represented with gradient bars (Fig. 2C). Moreover, the brightest N-cadherin clusters (yellow) in the SFB were strongly localized at the junction (Fig. 2C).

Real-time imaging in live cells showed a mobile state of N-cadherin molecules on the bridge between two cells (fig. S6 and movie S4). The mobile N-cadherin molecules moved to the cell body and then appeared to accumulate at the junction between the filopodium end and the cell body. This directional motion was correlated with a retrograde F-actin flow and led to a cluster at one end. Accordingly, we speculate that DFB0 evolves to DFB1 or DFB2, as the contact length and cadherin-cadherin binding frequency increase and eventually convert to an SFB held by N-cadherin clusters accumulated at the junction. This result proposes a molecular mechanism for how N-cadherin holds individual TNTs (*21*).

SFB as a close-ended TNT

TNT mediates intercellular calcium flux propagation between interconnected HeLa cell pairs (*13*). To evince that the SFB between HeLa cells satisfies the characteristics of conventional TNT, we investigated cell-to-cell propagation of intercellular calcium through the structure of SFB. Pointy ultraviolet (UV; 365 nm) light focus provoked transient calcium rise in a single cell by the exclusive uncaging of dimethoxynitrophenyl-EGTA-4 (DMNPE-4) AM-caged calcium while monitoring intercellular calcium mobilization in real time from the intensity alteration of Cal-520 AM, a calcium-sensitive fluorogenic indicator (Methods and fig. S7). FBs were distinguished into DFB or SFB by distributions of expressed N-cadherin–mScarlet-I, notably the existence of N-cadherin along the length (fig. S7A).

When we measured the Ca^{2+} indicator intensity changes of partner cells connected through FB during the uncaging on the target cell ($N_{cell\ pair} = 60$), a consequent rise that implicates intercellular calcium transfer was recognized mostly through SFBs (Fig. 3, A to C).

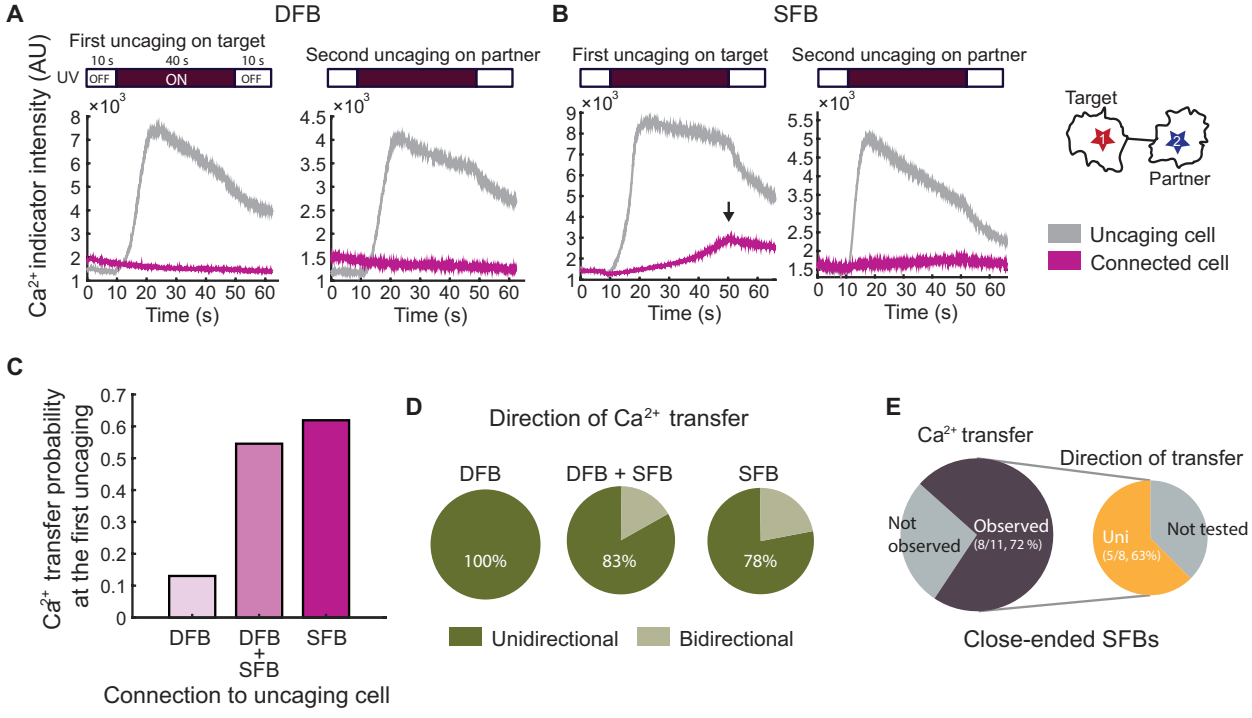

Fig. 3. Intercellular calcium transfer through HeLa SFB. Following selective uncaging of caged calcium (DMNPE-4) in a single cell by UV exposure (365 nm), calcium transfer to the connected cell through DFBs or SFBs was imaged by monitoring the intensity change of calcium indicator dye (Cal-520) in each cell (fig. S7 and Methods). (**A** and **B**) Representative intensity traces. While calcium indicator intensity increases markedly in the target cells by uncaging (40 s), the connected cell through DFB shows no intensity change, but correlated intensity increase was observed in the partner cell connected through SFB. Follow-up uncaging in the partner cell shows the directionality of Ca^{2+} transfer through DFBs. DFBs or SFBs were classified by N-cadherin distribution along their lengths. AU, arbitrary units. (**C**) Calcium transfer probability to partner cells at the first uncaging on target cells represent that most SFBs deliver calcium signal in contrast to DFBs ($N_{cell\ pairs} = 60$ from three independent experiments). (**D**) Direction of Ca^{2+} transfer invested at the second uncaging was unidirectional mostly on DFBs or SFBs ($N_{cell\ pairs} = 20$ from three independent experiments). (**E**) When only SFBs with confirmed terminal N-cadherin clusters were counted, they all transferred calcium unidirectionally.

Follow-up uncaging on the partner was accompanied selectively ($N_{cell\ pair}$ = 20) to further inspect the directionality of observed propagation. The results indicate that most calcium transfer is unidirectional regardless of DFB or SFB (Fig. 3, B and D). However, 22% of the SFBs having the bidirectional transfer of Ca^{2+} ions between cells might be an open-ended structure in TNTs (Fig. 3D). By spotlighting only the cells paired through SFB representing terminal N-cadherin cluster ($N_{cell\ pair}$ = 11), most SFBs channeled calcium propagation (72%) that was unidirectional between every cell pair tested for directionality ($N_{cell\ pair}$ = 5; Fig. 3E). This observation strongly suggests that SFB is a close-ended TNT connected by N-cadherin molecules. This unidirectional calcium transfer is improbable through an open-ended but a discriminative gate. From this point on, SFB will be referred to as TNT.

Helical deformation of DFBs

There seemed to be a particular structure of DFBs in living cell images (fig. S8 and movie S5), but diffraction-limited microscopy cannot resolve the fine form of DFBs. To characterize the nanoscale structures of DFBs, we used stochastic optical reconstruction microscopy (STORM) to image F-actin in various fixed cells (Fig. 4A, left) and two-color super-resolution radial fluctuation (SRRF) microscopy (*22*) in living HeLa cells expressing Lifeact-EGFP and Lifeact-mCherry (Fig. 4A, right). A double helical structure of DFB was shown in various cell lines. The half-pitch of the twisted DFB was 2.0 ± 0.9 μm on average (Fig. 4B). When DFBs longer than the helical pitch (shortest DFB = 5.4 μm) were observed for 1 to 2 hours after 36 to 48 hours of coculture, 66% of FBs were DFBs, and the remaining 34% were TNTs (Fig. 4C). Among DFBs in HeLa cells, 44% appeared to be twisted, and 56% of DFBs were not clear whether they were twisted (Fig. 4C). Some of the unresolved DFBs may have been changing to form a helical structure (Fig. 4C). In U2OS and human embryonic kidney–293 (HEK-293) cells, we could observe more TNTs than DFBs, but the ratio of twisted DFB to unresolved DFB was like that of HeLa cells (Fig. 4C).

Previous studies have shown that myosin V is involved in the F-actin rotation, resulting in filopodial rotation (*23*, *24*). To test the effect of myosin V on helical DFBs, siRNA was used to decrease the expression level of myosin Va or Vb. The specific down-regulation was confirmed by Western blotting (fig. S9). The occurrence of helical DFBs was markedly reduced when the expression level of myosin Va or Vb was lowered up to 83 or 73% in HeLa cells, respectively (Fig. 4D and fig. S9), which indicates that myosin V downgradation by siRNA is likely to affect the formation of the helical structure of DFB. This observation strongly suggests that the helical deformation of DFBs results from the F-actin rotation induced by myosin V. Moreover, during the transition of DFBs to TNTs, when one filopodium of the DFB is released from the cell body or the other filopodium, it is likely to be retracted rotationally (40:00; Fig. 1C, fig. S8, and movie S5). Filopodium retraction is expected to

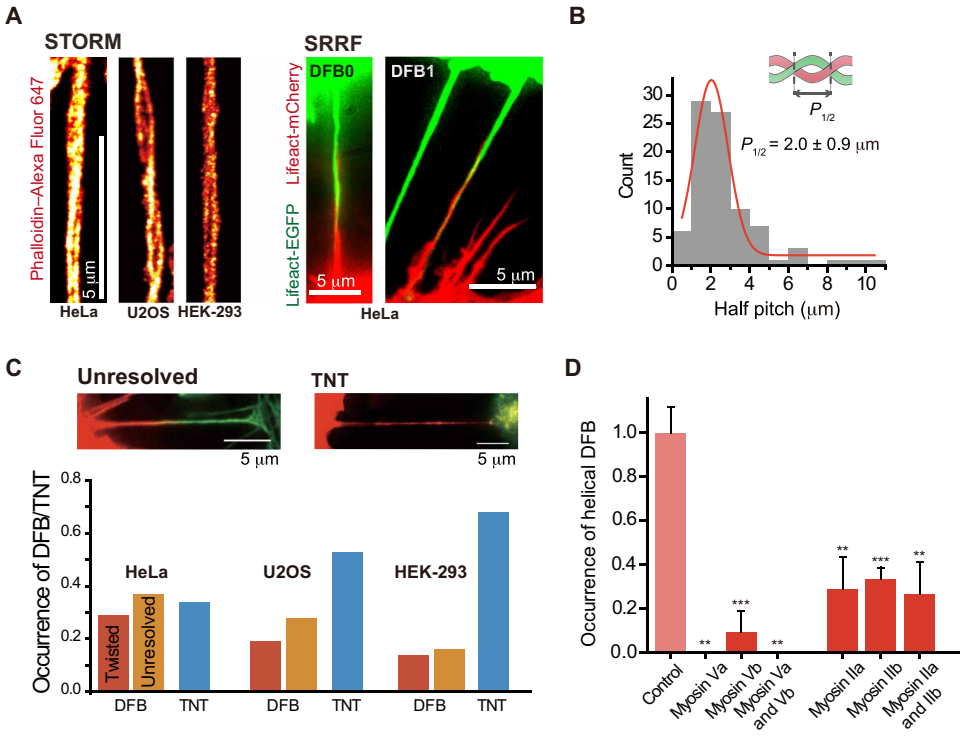

Fig. 4. Helical twisting of DFB in super-resolution microscopy. (**A**) Helical structures of DFBs were resolved in fixed HeLa, U2OS, and HEK-293 cells (fixed between 36 and 60 hour from seeding) by STORM using Alexa Fluor 647-phalloidin. DFB0 and DFB1 were imaged in living HeLa cells using a two-color SRRF microscopy. Lifeact-EGFP or Lifeact-mCherry was transfected into HeLa cells for F-actin staining. Images of living cells were taken 48 hours after cell seeding. (**B**) Helical structures were characterized by determining the half-pitch (the lengthwise interval between two intersections of protrusions: $n = 86$). The peak and width of each quantity were determined by Gaussian fitting. (**C**) Occurrence of DFB with or without the helical structure and TNT in living cells (HeLa: $n = 227$, $N_{\text{cell pair}} = 121$, U2OS: $n = 180$, $N_{\text{cell pair}} = 68$, and HEK-293: $n = 95$, $N_{\text{cell pair}} = 69$). "Unresolved" indicates that it is not clear whether the structure is twisted (see the top-left image). (**D**) Proportion of helical DFBs to DFBs was normalized and compared to investigate the contribution of myosin motors to twisting by knocking down the proteins with 60 nM siRNA ($N_{\text{DFB}} = 32$ for control, $N_{\text{DFB}} = 31$ for myosin Va, $N_{\text{DFB}} = 34$ for myosin Vb, $N_{\text{DFB}} = 75$ for myosin Va and Vb, $N_{\text{DFB}} = 68$ for myosin IIa, $N_{\text{DFB}} = 73$ for myosin IIb, and $N_{\text{DFB}} = 242$ for myosin IIa and IIb). $P = 0.00674$ for myosin Va, $P = 0.00084$ for myosin Vb, $P = 0.00674$ for myosin Va and Vb, $P = 0.00952$ for myosin IIa, $P = 0.00326$ for myosin IIb, and $P = 0.00538$ for myosin IIa and IIb by one-sided Student's t test. $^{**}P \leq 0.01$, $^{***}P \leq 0.005$. DFBs were imaged by SRRF microscopy of live HeLa cells expressing Lifeact-mNeonGreen and Lifeact–mScarlet-I.

be caused by F-actin retrograde flow by myosin II proteins. Our observation indicates that myosin II plays a critical role in the transition of DFBs into TNTs. The frequency of the helical deformation of DFBs significantly decreased in the cells in which myosin II was down-regulated by siRNA (Fig. 4D and fig. S9). Since myosin II proteins walk along helical actin filaments in lamellipodia (*25*, *26*), they seem to be involved in the helical formation of DFBs. However, their effect on helical deformation is less than that of the myosin V (Fig. 4D).

An elastic model of filopodial bridges

To address the physical validity of the helical deformation of DFBs, we studied the elastic properties of DFBs and TNTs using optical tweezers combined with LSCM (*17*). This correlative microscopy allowed us to distinguish TNTs from DFBs by two-color imaging. A biotinylated TAT (transactivated-transcripiton) peptide was attached to a streptavidin-coated microsphere of 1 μm in diameter using biotin-streptavidin interaction (Methods). The TAT peptide can penetrate the cell membrane and interact strongly with F-actin inside a DFB/TNT (*27*). A bead located at the center of the TNT or DFB was trapped and pulled perpendicular to the lengthwise axis (Fig. 5A and movie S6). The resulting force extension curves showed that the TNT (blue) extended notably longer than the DFB (purple) from any length at any given force (Fig. 5A), enabling determination of the bending moduli of the TNT and DFB.

To construct a physical model of DFBs/TNTs, we established a coarse-grained model for the filopodium as an elastic bundle of worm-like chains (WLCs) that can be bent and twisted by external forces and torques. We assumed that the filopodium consists of an inextensible seven WLC bundle composed of 50-nm beads in diameter (fig. S10). The effective Hamiltonian (H_{eff}) of the WLC bundle is defined by

$$H_{\text{eff}} = \sum_{i=1}^{7} H_{\text{WLC}}^{(i)} + H_{\text{bundle}} + U_{\text{exc}}$$

where $H_{\text{WLC}}^{(i)}$ is the bending energy of the ith WLC comprising the filopodium, H_{bundle} is the bundling interaction among the WLCs needed for the filopodium's twist and shear rigidities, and U_{exc} describes the excluded volume interactions among the beads (Supplementary Text). We carried out Langevin dynamics simulations of our coarse-grained model via the molecular dynamics simulator Large-scale Atomic/Molecular Massively Parallel Simulator (*28*). The force extension curve obtained from our filopodium model was found to excellently explain the corresponding experimental data in the range of forces from −20 to +20 pN (Fig. 5B and fig. S11). The persistence length of the TNT was estimated to be

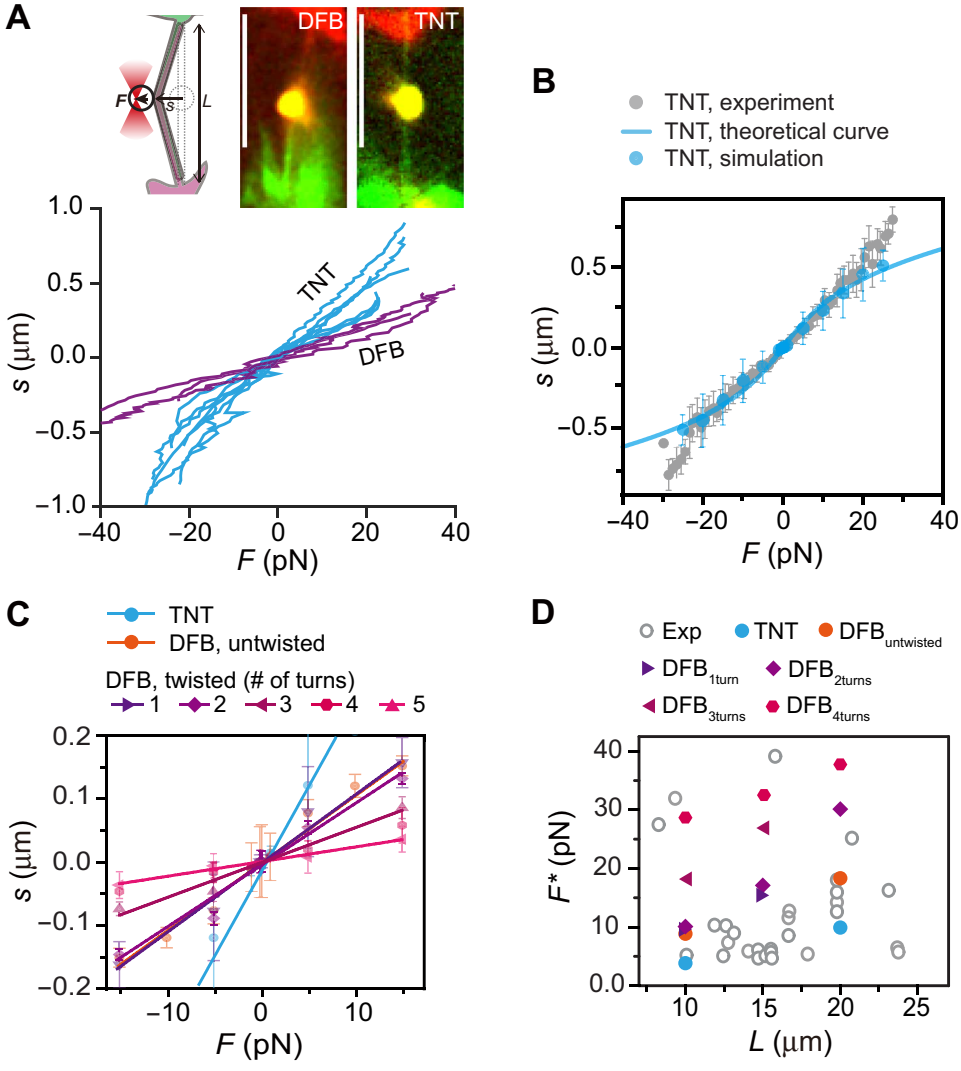

Fig. 5. Elastic properties of DFB/TNT. (**A**) Representative force extension curves of DFBs ($n = 3$ and $L = 9.4$, 15.6, and 20.8 μm) and TNTs ($n = 5$ and $L = 12.5$, 12.8, 14.7, 15.2, and 15.5 μm) using optical tweezers. +s, pulling to the right; −s: pulling to the left. Inset: Representative images of DFB/TNT in the pulling experiment. (**B**) The experimental force extension curve of TNTs (seven trajectory average) compared to the simulated extension curve (blue dots) and the theoretical response of a semiflexible filament subject to a force F (solid line; see Supplementary Text). The equation of motion was solved in units of the integration time step of 10 ns, with the bending modulus $k_b = 1.5 \times 10^2\ k_BT \cdot \mu m$, the stretching modulus $k_s = 3 \times 10^4\ k_BT/\mu m^2$, and the shear modulus $k_{sh} = 3 \times 10^4\ k_BT$ in H_{eff}. (**C**) Simulation results present the force extension relation of a TNT and DFBs with the helical turns from zero to five. (**D**) Force F^* to deform DFBs or TNTs by $s = 0.01\ L$ (L: the contour length at $F = 0$) in the experiment and simulations. The experimental data are plotted for DFBs of various L ranging from ~10 to ~25 μm. The simulation data show F^* for DFBs (or TNTs) of $L = 10$, 15, and 20 μm at zero to four helical turns.

1.0 μm by fitting to the data (Fig. 5B) with a WLC-based simple theory within that range (Supplementary Text).

Next, using the above filopodium model, a 10-μm-long helical DFB was constructed by interwinding two filopodia with each other and binding them via strong adhesion interactions at the filopodia ends. We observed that the DFB had a stiffer force extension curve proportional to the number of applied turns (Fig. 5C). We then measured the force F^* to deform the DFB by a distance of 1% of its total length ($s = 0.01 \times L$). The experimentally observed DFBs with a similar length exhibited a pronounced scatter in F^* (Fig. 5D), which is expected to occur due to the stiffness heterogeneity in DFBs with different numbers of turns. The DFBs with turns from 0 to 4 showed a similar scattered F^* in the simulation, consistent with the experiment.

After validating our model of the DFB in terms of elasticity, we modeled the cadherin-cadherin interaction on the contact surface in a DFB: N-cadherin clusters appeared as three consecutive monomers in one of the six outer WLCs (fig. S12). They were assumed to be randomly distributed along the DFB with an average separation of 1.4 (± 0.9) μm measured in our experiment (fig. S13). The adhesion strength of the binding monomer was determined such that the minimum helical pitch (namely, the maximum twist) made in our model DFB against the applied torque was identical to the value estimated from the experiment (Fig. 5D and fig. S12).

Model of DFB transition to a TNT

Using the above filopodium model, we examined how two filopodia form a helical DFB and transform into a TNT under cell-produced mechanical fluctuations. On the basis of our observation of the helical deformation of a DFB and the contraction in filopodia, the 10-μm-long DFB was stretched and twisted by a retractile force (f) and a torque (τ), respectively, which were applied to the starting end of each filopodium with equal magnitude but in the opposite directions (Fig. 6A, cartoon). We measured the number of helical turns in the DFB at a given retractile force and torque, displayed as a heat map in terms of f and τ (Fig. 6A). The computer-aided simulation results showed that the helicity and stability of the DFB sensitively depend on the applied mechanical force and torque: Under a force of $f < 7.3$ pN, the torque applied to the filopodia tends to render a stable helical DFB (movie S7), but beyond a force-dependent threshold torque, the helical structure of the DFB suddenly breaks down, and it appears to exist as two separate filopodia (movie S8). Similarly, a sufficiently large force resulted in a shear-induced disruption of the DFB beyond the torque-dependent threshold value. Outside the phase boundary (gray region), the applied torque or force plays a role in disrupting the helical DFB. The separated filopodia are then believed to be contracted to their own cell body by the retraction force if the growing ends are not attached to the opposite cell membranes. The 90% of filopodial retraction force that we measured using optical tweezers were less than 8.0 pN (fig. S14) (*17*), which is consistent with our simulation and similar to a previously reported result in a mouse macrophage (84% less than 8.0 pN) (*29*). Moreover, since most retraction forces are lower than 5 pN (fig. S14), a torque is required to break the interaction between two filopodia (Fig. 6). Together, these results indicate that the helical deformation of the DFB leads to the separation of two filopodia from the DFB, which results in the transformation of a DFB into a TNT.

The transition of a DFB0 to a TNT via a DFB1, which we have observed (Fig. 1C and fig. S8), strongly suggests that the asymmetric growth rate of the filopodia's free ends in a DFB is essential. Consequently, one of the filopodia reaches and anchors in the opposite cell body with a faster growth rate, while the other filopodium does not. This creates the different boundary conditions of the two filopodia ends for rotation: The membrane-anchored filopodium is rotationally fixed in space, while the other filopodium is free from such restriction (Fig. 6B, cartoon). For various conditions of f and τ, we obtained the stability phase diagram of a DFB1 as a function of the retractile force and the torque (Fig. 6B, red curve). For comparison, the phase diagram of the DFB0 consisting of two free end filopodia in Fig. 6A was overlaid (black line). Unexpectedly, we found a marked effect of the retractile force on the DFB-to-TNT transition in DFB1 compared to the DFB0; the retractile force can promote the formation of TNTs under a broader range of conditions (the shaded region; Fig. 6B and movie S9). In particular, the role of the force in the TNT transition became pronounced in the small-torque regime. With a typically measured retractile force of <8 pN in our experiment, the cells can mechanically disrupt the interwound DFB conformation. While the unanchored filopodium is retracted back to the cell body in the separation process, the anchored filopodium remains a bridge and lastly forms a TNT.

DISCUSSION

Here, we have studied a transition of DFB to SFB suspended between cells. Unidirectional calcium propagation through transformed SFB denotes that this structure is a close-ended TNT. The DFB helicity

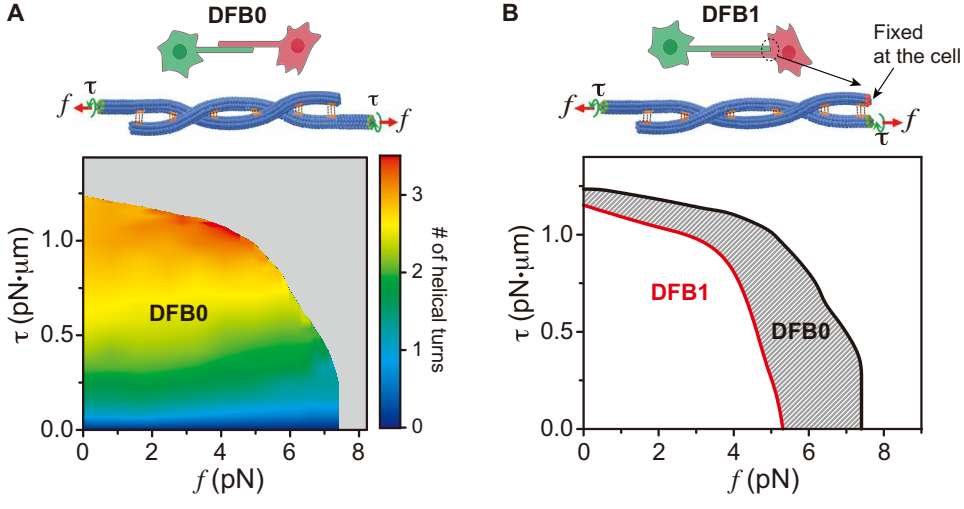

Fig. 6. The DFB-to-TNT transition in the simulation. (**A**) A DFB with a contact length of 10 μm was constructed with two opposing filopodia with randomly distributed binding sites, with an average separation of 1.4 ± 0.9 μm (fig. S13). The filopodia of a DFB0 were pulled and twisted by a retractile force (f) and a torque (τ), respectively. The plotted heatmap shows the number of helical turns in the DFB0 as a function of the applied f and τ. The disruption point makes a phase boundary line starting from (f, τ) = (0 pN, 1.25 pN·μm) to (7.3 pN, 0 pN·μm). The gray region ($\tau > 1.25$ pN·μm or $f > 7.3$ pN) indicates the phase in which the DFB0 was disrupted into two separate filopodia upon the applied force and torque. (**B**) Phase diagram showing the DFB-to-TNT transition in two distinct situations. The red curve corresponds to the disruption line for a DFB1 in which one of the filopodia is anchored in the opposite cell body and a rotationally fixed state. The black curve is for DFB0 in (A), where the growing ends of both filopodia were rotationally free. DFB1 with a fixed end can be more easily disrupted into a TNT with a lower retractile force, especially in the small torque regime. The shaded region indicates the enhanced TNT-driven mechanical condition due to rotation fixation. It can be inferred that DFB can mechanically transform into TNT at retractile cytoskeletal forces of <8 pN. The phase diagram was obtained from the simulation data of >200 at every grid point of (f, τ).

and the filopodia retraction, which are produced by the torque and force applied by myosin V and/or myosin II to the F-actin inside the filopodia (Fig. 4D), lead to the DFB-to-TNT transition; the torsional and shearing energies accumulated in the helical DFB dominate the total adhesion energy between the filopodia. As expected, the occurrence of TNTs significantly decreased in myosin II knockdown cells and in cells treated with blebbistatin, an inhibitor of the adenosine triphosphatase (ATPase) activity of myosin II (fig. S15A). However, the knockdown of myosin V and treatment with Myovin-1 (an inhibitor of the myosin V ATPase activity) did not affect the frequency of TNT formation (fig. S15B). A possible interpretation is that the weaker torque of myosin II may be sufficient to break the N-cadherin interaction between the two filopodia when one of the filopodia is rotationally fixed at the paired cell membrane due to the asymmetrical elongation of the filopodia (Fig. 6).

The extracellular interaction between N-cadherin molecules on two distinct filopodia linked to β-catenin sustains the physical contact between the filopodia in DFBs (fig. S16). Since the N-cadherin/β-catenin complex inhibits F-actin retrograde flow (*30*), it can direct the growth of filopodia in a DFB. The N-cadherin/β-catenin cluster formed at the filopodium end provides a strong bond between the end of the filopodium and the paired cell membrane. Together with the unidirectional transfer of Ca^{2+} ions through TNTs (Fig. 3), the N-cadherin cluster is most likely to form close-ended TNTs connecting the paired cell body. Excitingly, a recent study showed that interpericyte cells in the mouse retina communicate through gap junctions at the ends of close-ended TNTs (*31*).

Our studies propose a model of how a close-ended TNT is formed from a helically deformed DFB (fig. S17). Two filopodia that protrude from cells involved in cell-to-cell communication appear to make physical contact through N-cadherin molecules anchored to F-actin via catenin molecules (DFB0). A high density of N-cadherin/catenin complexes inhibits retrograde F-actin flow. Instead, the filopodia are extended by actin polymerization until the filopodium reaches the paired cell body. The torsional energy conferred to F-actin by myosin V and myosin II results in the helical structure of the DFB. The force and torque to break the N-cadherin/N-cadherin bonds between filopodia are lowered in DFB1. The accumulated torsional energy forces the two filopodia to separate. One filopodium is released and retracted. The cluster of N-cadherin/catenin complexes holds the TNT at the junction and forms a synaptic structure between the TNT and the paired cell body.

METHODS

Fluorescence microscopy

Video-rate LSCM was used for fluorescence imaging, as previously described (*32*). We collected the emissions from excited fluorophores through a 60× water-immersion [Olympus UPlanSApo 60×, numerical aperture (NA) = 1.2] or 100× oil-immersion objective (Olympus UPlanSApo 100×, NA = 1.4) on an inverted microscope (Olympus IX51). For multicolor excitation, up to four different lasers (Cobolt diode laser module (MLD), 405 nm, 100 mW; Cobolt MLD, 488 nm, 60 mW; CNI diode-pumped solid-state (DPSS) laser, 561 nm, 200 mW; and Cobolt MLD, 638 nm and 100 mW) were introduced sequentially (for the formation-transition study and time-lapse imaging of N-cadherin) using mechanical shutters (Uniblitz, LS3S2T0, and VMM-D3) or simultaneously (for the other multicolor imaging). Different excitation and emission wavelengths were reflected and transmitted through a quad-edge dichroic beam splitter (Semrock, Di01-R405/488/561/635). Galvano scanning mirrors (15 mm; Cambridge Technology, 6231H) were controlled using a homebuilt control program (LabVIEW). The emission signals were separated temporally through a multiple bandpass filter (Semrock, FF01-515/588/700-25) or spatially through a DV2 multichannel imaging system (Photometrics) with suitable bandpass filters (510/20 for Alexa Fluor 488, 600/37 for Alexa Fluor 568, and 680/40 for Alexa Fluor 647; Semrock) for simultaneous multiple excitations in front of an electron-multiplying charge-coupled device (EMCCD) camera (Andor iXon or iXon Ultra). Separated signals were obtained using imaging software (Solis or MetaMorph) with a time resolution of 100 ms. For the time-lapse experiment using multiple sequential excitations, the time interval was mainly set to 9.9 s for 60 to 180 min. A heated sample stage and a CO_2 supply system (Live Cell Instrument) were used to maintain cell viability during live-cell imaging. The image sequences obtained from the imaging program were analyzed using ImageJ and MATLAB (MathWorks) software. To overlay multicolor images of simultaneous multiple excitations, fluorescent bead images were recorded as a reference for mapping. Images were occasionally walking averaged over every four frames. For two-color SRRF imaging, we obtained 100 to 300 sequential images of each channel, analyzed them using the NanoJ-SRRF plug-in of ImageJ (*22*), and overlaid them using a MATLAB script.

Alternatively, highly inclined and laminated optical sheet (HiLo) microscopy was also used for stochastic optical reconstruction microscopy (STORM) or SRRF imaging. The microscope was built on an inverted Olympus IX71 microscope. The thin optical sheet of excitation beams (CNI diode laser, 405 nm, 50 mW; CNI DPSS laser, 561 nm, 200 mW; and Cobolt MLD, 638 nm, 180 mW) was generated through a 100× oil-immersion objective (Olympus UPlanSApo 100×, NA = 1.4) or 60× oil-immersion objective (Olympus ApoN 60×, NA = 1.49). The emission signals passing through a DV2 multichannel imaging system (Photometrics) with bandpass filters (600/37 for Alexa Fluor 568 and 676/37 for Alexa Fluor 647; Semrock) were collected through the 100× oil-immersion objective and captured by an EMCCD (Andor iXon 897) at a 10- to 30-Hz rate.

STORM imaging

STORM imaging was performed under LSCM with an objective (Olympus UPlanSApo 100×, NA = 1.4, oil immersion), resulting in a pixel size of 120 nm by 120 nm or HiLo microscopy with the same objective. Actin filaments labeled with Alexa Fluor 647-phalloidin were imaged with a 10- to 30-Hz frame rate for 5000 to 20,000 frames. Before STORM imaging, we used weak excitation (0.04 to 0.1 kW/cm^2, LSCM) with a 638-nm DPSS laser to visualize FBs or TNTs. We increased the excitation power (~3.5 kW/cm^2, LSCM) for STORM imaging to rapidly deactivate the fluorophores and enhance the positional accuracy by increasing the number of emitted photons per frame. A 405-nm laser with a weak excitation power (0 to 0.35 kW/cm^2) was used to reactivate the fluorophores from the dark state back to the fluorescent state. The acquired images were analyzed with the ImageJ plug-in ThunderSTORM (*33*) to measure the centroid positions from the switching spots. The analyzed localization data were rendered with the normalized Gaussian option in ThunderSTORM with a pixel size of 10 nm by 10 nm. The background noise was filtered for the optimal imaging condition. The *X*-*Y* drift was corrected using the cross-correlation function or a fluorescent bead (T7279, Invitrogen) fiducial marker. The images were colored with ImageJ Red Hot. For F-actin labeling, the cells were

fixed with 4% paraformaldehyde in cytoskeleton-protective buffer and then reduced with a fresh 0.1% (w/v) sodium borohydride (Sigma-Aldrich) solution for 7 min. After a 0.5- to 1-hour blocking step with 5% (w/v) bovine serum albumin (BSA; Sigma-Aldrich) at room temperature, the cells were incubated with a 200 to 400 nM Alexa Fluor 647-phalloidin (Thermo Fisher Scientific) solution overnight at 4°C. The labeled samples were rinsed once with phosphate-buffered saline (PBS). The imaging buffer was 100 to 200 mM β-mercaptoethanol, 2 mM Trolox, 2.5 mM protocatechuic acid, and 50 nM protocatechuate 3,4-dioxygenase in PBS or 100 mM β-mercaptoethylamine, 1 mM cyclooctatetraene, 100 mM sodium DL-lactate, and 3% oxyrase in PBS.

Cell culture

The immortalized cell lines HeLa [Korean Cell Line Bank (KCLB) or American Type Culture Collection for Ca^{2+} transfer], HEK-293 (KCLB), and U2OS (gifted from Y. K. Kim's laboratory, Korea University or KCLB) were cultured in phenol red–free Dulbecco's modified Eagle's medium (DMEM) to reduce autofluorescence or changed to phenol red–free DMEM (or live-cell imaging solution; Invitrogen) before imaging [10% fetal bovine serum (FBS), 1× penicillin-streptomycin, 1× GlutaMAX, or 1× MycoZap; Takara]. Cells were subcultured before they reached 90% confluence and used for experiments when their passage number was more than 3. All the cells we used were tested or newly purchased to avoid mycoplasma contamination.

Actin and membrane staining

For HeLa F-actin labeling, 1 μg of the *Lifeact-EGFP* (lab modification) or *Lifeact-mCherry* plasmid (Addgene) (*16*) was transfected into cells and incubated for 24 hours after subculturing (50 to 60% confluence) using 2 μl of the Lipofectamine 3000 reagent (Thermo Fisher Scientific) on 35-mm dishes. The transfection medium was changed after 12 hours of transfection. Alternatively, HeLa cells on 35-mm tissue culture dishes (SPL Life Sciences) with more than 50% confluency were transfected with a mixture of 3 μl of FuGENE (Promega), 30 μl of Opti-MEM (minimal essential medium; Gibco), and 1 μg of *Lifeact-mNeonGreen* or *Lifeact–mScarlet-I* mixture. The transfected cells on both dishes were trypsinized 24 hours after the medium change and collected into a 15-ml conical tube for gentle centrifugation (2 min, 145*g*). After the supernatants were removed, the cells were suspended in different volumes of the medium in a poly(dimethylsiloxane) (PDMS) chamber for live-cell imaging (*17*) or a glass-bottom dish (fixed cell or live-cell imaging; Cellvis) to control the cell density. We mixed the cells by repeatedly dispensing them and then injected the mixed cells, generally 400 μl into a PDMS chamber or 1.5 ml into a glass-bottom dish for imaging. For membrane labeling, DiI and DiD (Molecular Probes) were diluted to 5 μM in medium, used to treat cells on 35-mm dishes (24 hours after subculture) separately for 8 min, and then washed out according to the manufacturer's protocol. The cells were immediately mixed and moved to a PDMS chamber or 1.5 ml into a glass-bottom dish for imaging. The cells were imaged 36 to 60 hours after mixing and seeding. The medium was replaced with TNT formation-stimulating medium [2.5% FBS in DMEM and 50 mM glucose (pH 6.6 to 7.0)] (*10*) 12 to 24 hours after cell seeding. For fixed cell imaging, the cells were fixed with 4% paraformaldehyde in cytoskeleton-preserving buffer [80 mM Pipes (pH 6.8), 5 mM EGTA, and 2 mM $MgCl_2$] for 10 min, washed with PBS, and imaged in PBS.

Several studies have shown that Lifeact has severe actin defects (*34*, *35*) and affects F-actin arrangement and dynamics in vivo (*36*) at its high expression level. The constructs of Lifeact that we have used are as follows: promoter (pCMV)–EGFP-linker(SGLRSRAQASNS)–Lifeact, pCMV-Lifeact–linker(GDPPVAT)–mNeonGreen, pCMV-Lifeact-linker(GDPPVAT)–mCherry, and pCMV-Lifeact–linker(GDPPVAT)–mScarlet-I. The construct of Lifeact-mNeonGreen, Lifeact-mCherry, or Lifeact–mScarlet-I has no significant defects in the mild dose condition (*34*). From the image of F-actin in living cells and fixed cells using SiR-actin and phalloidin, we have not observed any difference between these probes and Lifeact in the dynamics and morphology of F-actin, the helical structure of DFB, and N-cadherin clusters at the end of SFB.

N-cadherin imaging

For the two-color imaging of cadherin, HeLa cells were transfected with *N-cadherin–mScarlet-I* or *N-cadherin–EGFP* plasmids to label the two-color F-actin. For real-time imaging of N-cadherin dynamics, N-cadherin was labeled with an anti–N-cadherin antibody conjugated to Alexa Fluor 488 or Alexa Fluor 647 (clone 8C11, BD). Two microliters of Alexa Fluor 488- or Alexa Fluor 647-conjugated anti–N-cadherin antibodies was diluted with 300 μl of the medium. For living cells, F-actins were incubated with 200 nM SiR-actin (Spirochrome) for 3 hours at 37°C; Alexa Fluor 488- or Alexa Fluor 647-conjugated anti–N-cadherin antibody and SiR-actin were then simultaneously injected, and the cells were incubated in the imaging chamber for 30 min at 37°C. After washing twice with prewarmed PBS, the cells were imaged with 200 nM SiR-actin to maintain F-actin labeling during time-lapse imaging. For fixed cell imaging, after the cells were incubated with an Alexa Fluor 488- or Alexa Fluor 647-conjugated anti–N-cadherin antibody and an Alexa Fluor 568-conjugated anti–β-catenin antibody (E247, Abcam) for 30 min at 37°C, the unbound antibodies were washed out. The cells were fixed with 4% paraformaldehyde in the cytoskeleton-preserving buffer. The fixed cells were rinsed with PBS and then permeabilized with 0.5% Triton X-100 (Sigma-Aldrich) in PBS for 10 min after a 0.5- to 1-hour blocking step with 5% (w/v) BSA (Sigma-Aldrich) at room temperature. For colabeling of F-actin, the fixed cells were additionally incubated in a 200 to 400 nM Alexa Fluor 647-phalloidin (Thermo Fisher Scientific) solution overnight at 4°C.

Down-regulation of proteins

To down-regulate endogenous N-cadherin or myosin proteins, cells were transfected with 60 nM in vitro–synthesized siRNAs (three target-specific 19 to 25 nucleotides; Santa Cruz Biotechnology) using Oligofectamine or Lipofectamine 2000 reagent (Thermo Fisher Scientific) in Opti-MEM. For imaging, cells grown on dishes were fixed 72 hours after transfection (see figs. S3 and S9 for more details).

Single-cell calcium uncaging experiment

HeLa cells were prepared to express N-cadherin–mScarlet-I in the TNT-stimulating condition as described above. After 48 hours from transfection (20 hours in TNT-stimulating condition), we incubated cells in dye-working media [20 μM DMNPE-4 AM-caged calcium (Tocris Bioscience), 5 μM Cal-520 AM (AAT Bioquest), 0.1% Pluronic F-127 (Sigma-Aldrich), 1 μM SiR-actin, and 10 μM verapamil (both from Cytoskeleton Inc.) in TNT-stimulation DMEM] for 1 hour (37°C). After the incubation, cells were moved to a stage-top incubating system (37°C, 5% CO_2; Tokai Hit) and imaged in imaging buffer [FluoroBrite DMEM supplied with 2.5% FBS and 1× GlutaMAX

(all from Gibco)]. Uncaging UV was exposed on the target cells for 40 s, either continuously or (10-s exposure and 3-s pause) by 30× (UPLSAPO30XS, NA = 1.05) or 60× silicone-oil immersion objectives (Olympus UPLSAPO60XS2, NA = 1.3).

Briefly introducing, homebuilt microscope (IX83, Olympus) with imaging lasers for inclined illumination (405, 488, 561, and 637 nm; OBIS CellX Laser System, Coherent) and a light-emitting diode light source for UV focus (365 nm; M365L2, Thorlabs) was used for this experiment. The pinhole (200 μm; Thorlabs) placed in a conjugated plane of the front focal plane of objectives confined UV light in the pointy focus [full width at half maximum (FWHM) = 23.6 μm for 30× objectives or FWHM = 12.0 μm for 60× objectives] for single-cell uncaging. We calculate the intensity of UV after passing the objectives to be ~1.0 and ~4.0 nW/μm^2 for 30× and 60× objectives, respectively. We used iXon Life 888 (Andor) for image acquisition. The whole imaging process was controlled on MetaMorph software (Molecular Devices).

Local correlation between N-cadherin/N-cadherin

We measured the intensities of N-cadherin–EGFP (I_{EGFP}) and N-cadherin–mScarlet-I (I_{mSca}) on the DFBs or TNTs between cells and subtracted the background intensity from the colocalization image. The local Pearson's correlation was measured at each pixel i [$L\_corr(i)$] using the mean (m) and the SD (s) of each profile

$$L\_corr(i) = \frac{[I_{EGFP}(i) - \mu_{EGFP}][I_{mSca}(i) - \mu_{mSca}]}{[n-1]\, s_{EGFP}\, s_{mSca}}$$

Force probe preparation

The force probe for the experiment was prepared. Ten microliters of streptavidin-coated polystyrene beads, 1 μm in diameter with fluorescein isothiocyanate coating (stock concentration ~31 pM; Bangs Laboratories), was washed twice by diluting the beads in PBS, vertexing, sonicating, and centrifuging (19,000g for 10 min). In the last washing step, the beads were suspended in 9 μl of PBS, and 1 μl of a biotin-TAT peptide (stock concentration of ~500 μM; AnaSpec) was added. After 30 min of incubation with gentle shaking, the beads were washed three times and resuspended in 100 μl of PBS (final concentration of ~3.1 pM).

Measurement of the force extension curve of DFB/TNT using optical tweezers

The details of the experimental setup and necessary procedure were described in our previous report (*17*). HeLa cells were transfected to express Lifeact-GFP or Lifeact-mCherry and seeded in PDMS. After more than 24 hours, TAT-coated beads diluted to 4 to 5 fM in cell culture medium were introduced. JPK NanoTracker Desktop Software was used to manage the optical tweezers (NanoTracker 2, JPK Instruments AG) to trap a TAT bead and bind it to a DFB/TNT. At the same time, homebuilt LSCM was used to visualize the fluorescence of FBs to distinguish DFBs from TNTs. The trap stiffness of TAT-coated beads was calibrated to 0.01 pN/nm under our experimental conditions. The trapped and calibrated microspheres were attached to the center of the target a DFB/TNT by moving the stage upward to the trapping focus. After the binding was confirmed by the reduced fluctuation of the axial force signal, the trap was moved orthogonally to the lengthwise axis to deform the linked DFB/TNT (maximum displacement = 3 μm and moving speed = 0.3 μm/s). Measured force signals were analyzed using MATLAB scripts.

SUPPLEMENTARY MATERIALS

Supplementary material for this article is available at https://science.org/doi/10.1126/sciadv.abj3995

REFERENCES AND NOTES

1. A. Rustom, R. Saffrich, I. Markovic, P. Walther, H. H. Gerdes, Nanotubular highways for intercellular organelle transport. *Science* **303**, 1007–1010 (2004).
2. B. Önfelt, S. Nedvetzki, R. K. P. Benninger, M. A. Purbhoo, S. Sowinski, A. N. Hume, M. C. Seabra, M. A. A. Neil, P. M. W. French, D. M. Davis, Structurally distinct membrane nanotubes between human macrophages support long-distance vesicular traffic or surfing of bacteria. *J. Immunol.* **177**, 8476–8483 (2006).
3. P. Veranic, M. Lokar, G. J. Schutz, J. Weghuber, S. Wieser, H. Hagerstrand, V. Kralj-Iglic, A. Iglic, Different types of cell-to-cell connections mediated by nanotubular structures. *Biophys. J.* **95**, 4416–4425 (2008).
4. B. Önfelt, S. Nedvetzki, K. Yanagi, D. M. Davis, Cutting edge: Membrane nanotubes connect immune cells. *J. Immunol.* **173**, 1511–1513 (2004).
5. N. M. Sherer, M. J. Lehmann, L. F. Jimenez-Soto, C. Horensavitz, M. Pypaert, W. Mothes, Retroviruses can establish filopodial bridges for efficient cell-to-cell transmission. *Nat. Cell Biol.* **9**, 310–315 (2007).
6. M. Inaba, M. Buszczak, Y. M. Yamashita, Nanotubes mediate niche-stem-cell signalling in the Drosophila testis. *Nature* **523**, 329–332 (2015).
7. Y. Connor, S. Tekleab, S. Nandakumar, C. Walls, Y. Tekleab, A. Husain, O. Gadish, V. Sabbisetti, S. Kaushik, S. Sehrawat, A. Kulkarni, H. Dvorak, B. Zetter, E. R. Edelman, S. Sengupta, Physical nanoscale conduit-mediated communication between tumour cells and the endothelium modulates endothelial phenotype. *Nat. Commun.* **6**, 8671 (2015).
8. G. Haimovich, C. M. Ecker, M. C. Dunagin, E. Eggan, A. Raj, J. E. Gerst, R. H. Singer, Intercellular mRNA trafficking via membrane nanotube-like extensions in mammalian cells. *Proc. Natl. Acad. Sci. U.S.A.* **114**, E9873–E9882 (2017).
9. F.-A. Ramírez-Weber, T. B. Kornberg, Cytonemes. *Cell* **97**, 599–607 (1999).
10. E. Lou, S. Fujisawa, A. Morozov, A. Barlas, Y. Romin, Y. Dogan, S. Gholami, A. L. Moreira, K. Manova-Todorova, M. A. S. Moore, Tunneling nanotubes provide a unique conduit for intercellular transfer of cellular contents in human malignant pleural mesothelioma. *PLOS ONE* **7**, e33093 (2012).
11. D. Wittig, X. Wang, C. Walter, H.-H. Gerdes, R. H. W. Funk, C. Roehlecke, Multi-level communication of human retinal pigment epithelial cells via tunneling nanotubes. *PLOS ONE* **7**, e33195 (2012).
12. L. Gonzalez-Mendez, I. Seijo-Barandiaran, I. Guerrero, Cytoneme-mediated cell-cell contacts for Hedgehog reception. *eLife* **6**, e24045 (2017).
13. K. Hase, S. Kimura, H. Takatsu, M. Ohmae, S. Kawano, H. Kitamura, M. Ito, H. Watarai, C. C. Hazelett, C. Yeaman, H. Ohno, M-Sec promotes membrane nanotube formation by interacting with Ral and the exocyst complex. *Nat. Cell Biol.* **11**, 1427–1432 (2009).
14. D. Cordero Cervantes, C. Zurzolo, Peering into tunneling nanotubes–The path forward. *EMBO J.* **40**, e105789 (2021).
15. N. Leijnse, L. B. Oddershede, P. M. Bendix, Helical buckling of actin inside filopodia generates traction. *Proc. Natl. Acad. Sci. U.S.A.* **112**, 136–141 (2015).
16. J. Riedl, A. H. Crevenna, K. Kessenbrock, J. H. Yu, D. Neukirchen, M. Bista, F. Bradke, D. Jenne, T. A. Holak, Z. Werb, M. Sixt, R. Wedlich-Soldner, Lifeact: A versatile marker to visualize F-actin. *Nat. Methods* **5**, 605–607 (2008).
17. M. Chang, J. Oh, Y. Kim, S. Hohng, J.-B. Lee, Extended depth of field for single biomolecule optical imaging-force spectroscopy. *Opt. Express* **25**, 32189–32197 (2017).
18. M. Lokar, A. Iglič, P. Veranič, Protruding membrane nanotubes: attachment of tubular protrusions to adjacent cells by several anchoring junctions. *Protoplasma* **246**, 81–87 (2010).
19. M. Chang, J. Oh, J. Doh, J.-B. Lee, F-actin dynamics transform filopodial bridges into intercellular nanotubes capable of distant cell communication. *bioRxiv* 10.1101/405340 (2018).
20. S. A. Kim, C.-Y. Tai, L.-P. Mok, E. A. Mosser, E. M. Schuman, Calcium-dependent dynamics of cadherin interactions at cell–cell junctions. *Proc. Natl. Acad. Sci. U.S.A.* **108**, 9857–9862 (2011).
21. A. Sartori-Rupp, D. Cordero Cervantes, A. Pepe, K. Gousset, E. Delage, S. Corroyer-Dulmont, C. Schmitt, J. Krijinse-Locker, C. Zurlolo, Correlative cryo-electron microscopy reveals the structure of TNTs in neuronal cells. *Nat. Commun.* **10**, 342 (2019).
22. N. Gustafsson, S. Culley, G. Ashdown, D. M. Owen, P. M. Pereira, R. Henriques, Fast live-cell conventional fluorophore nanoscopy with ImageJ through super-resolution radial fluctuations. *Nat. Commun.* **7**, 12471 (2016).
23. A. Tamada, S. Kawase, F. Murakami, H. Kamiguchi, Autonomous right-screw rotation of growth cone filopodia drives neurite turning. *J. Cell Biol.* **188**, 429–441 (2010).
24. N. Leijnse, Y. F. Barooji, M. R. Arastoo, S. L. Sønder, B. Verhagen, L. Wullkopf, J. T. Erler, S. Semsey, J. Nylandsted, L. B. Oddershede, A. Doostmohammadi, P. M. Bendix, Filopodia rotate and coil by actively generating twist in their actin shaft. arXiv:2111.13127 (2021).

25. J. F. Beausang, H. W. Schroeder III, P. C. Nelson, Y. E. Goldman, Twirling of actin by myosins II and V observed via polarized TIRF in a modified gliding assay. *Biophys. J.* **95**, 5820–5831 (2008).
26. T. Wakatsuki, R. B. Wysolmerski, E. L. Elson, Mechanics of cell spreading: Role of myosin II. *J. Cell Sci.* **116**, 1617–1625 (2003).
27. A. Mishra, G. H. Lai, N. W. Schmidt, V. Z. Sun, A. R. Rodriguez, R. Tong, L. Tang, J. Cheng, T. J. Deming, D. T. Kamei, G. C. L. Wong, Translocation of HIV TAT peptide and analogues induced by multiplexed membrane and cytoskeletal interactions. *Proc. Natl. Acad. Sci. U.S.A.* **108**, 16883–16888 (2011).
28. S. Plimpton, Fast parallel algorithms for short-range molecular-dynamics. *J. Comput. Phys.* **117**, 1–19 (1995).
29. H. Kress, E. H. K. Stelzer, D. Holzer, F. Buss, G. Griffiths, A. Rohrbach, Filopodia act as phagocytic tentacles and pull with discrete steps and a load-dependent velocity. *Proc. Natl. Acad. Sci. U.S.A.* **104**, 11633–11638 (2007).
30. L. Bard, C. Boscher, M. Lambert, R.-M. Mege, D. Choquet, O. Thoumine, A molecular clutch between the actin flow and N-cadherin adhesions drives growth cone migration. *J. Neurosci.* **28**, 5879–5890 (2008).
31. L. Alarcon-Martinez, D. Villafranca-Baughman, H. Quintero, J. B. Kacerovsky, F. Dotigny, K. K. Murai, A. Prat, P. Drapeau, A. D. Polo, Interpericyte tunnelling nanotubes regulate neurovascular coupling. *Nature* **585**, 91–95 (2020).
32. J. Lee, Y. Miyanaga, M. Ueda, S. Hohng, Video-rate confocal microscopy for single-molecule imaging in live cells and superresolution fluorescence imaging. *Biophys. J.* **103**, 1691–1697 (2012).
33. M. Ovesny, P. Krizek, J. Borkovec, Z. Svindrych, G. M. Hagen, ThunderSTORM: A comprehensive ImageJ plug-in for PALM and STORM data analysis and super-resolution imaging. *Bioinformatics* **30**, 2389–2390 (2014).
34. L. R. Flores, M. C. Keeling, X. Zhang, K. Sliogeryte, N. Gavara, Lifeact-TagGFP2 alters F-actin organization, cellular morphology and biophysical behaviour. *Sci. Rep.* **9**, 3241 (2019).
35. N. Courtemanche, T. D. Pollard, Q. Chen, Avoiding artefacts when counting polymerized actin in live cells with LifeAct fused to fluorescent proteins. *Nat. Cell Biol.* **18**, 676–683 (2016).
36. A. J. Spracklen, T. N. Fagan, K. E. Lovander, T. L. Tootle, The pros and cons of common actin labeling tools for visualizing actin dynamics during Drosophila oogenesis. *Dev. Biol.* **393**, 209–226 (2014).
37. G. Lukinavičius, L. Reymond, E. D'Este, A. Masharina, F. Gottfert, H. Ta, A. Guther, M. Fournier, S. Rizzo, H. Waldmann, C. Blaukopf, C. Sommer, D. W. Gerlich, H.-D. Arndt, S. W. Hell, K. Johnsson, Fluorogenic probes for live-cell imaging of the cytoskeleton. *Nat. Methods* **11**, 731–733 (2014).
38. M. Nakanishi, R. R. Mitchell, Y. D. Benoit, L. Orlando, J. C. Reid, K. Shimada, K. C. Davidson, Z. Shapovalova, T. J. Collins, A. Nagy, M. Bhatia, Human pluripotency is initiated and preserved by a unique subset of founder cells. *Cell* **177**, 910–924.e22 (2019).

Acknowledgments

Funding: This research was supported by the National Research Foundation of Korea funded by the Ministry of Science and ICT (2021R1I1A1A01059649 to O.-c.L., 2020R1A2C4002490 to J.-H.J., and 2017K1A1A2013241 to J.-B.L.) and LG Yonam Foundation of Korea (to J.-B.L.). This work was also supported by the National Institutes of Health grant DP1MH119428 (to H.-B.K.). We are grateful for the support of POSTECH Basic Research Science Center. **Author contributions:** M.C. and J.-B.L. conceived the project. M.C., G.B., and J.O. performed all the experiments. O.-c.L. and J.-H.J. performed the computer-aided simulation and developed the theoretical model. N.-O.Y. and S.H.R. helped cell cultures and provided materials. H.-B.K. and J.D. contributed to critical discussion and provided materials. A.B.K. and S.-H.S. contributed to data analysis and critical discussion. M.C., O.-c.L., G.B., J.-H.J., and J.-B.L. wrote the paper. All authors contributed to data analysis and edited the manuscript. **Competing interests:** The authors declare that they have no competing interests. **Data and materials availability:** All data needed to evaluate the conclusions in the paper are present in the paper and/or the Supplementary Materials.

Submitted 10 May 2021
Accepted 5 February 2022
Published 30 March 2022
10.1126/sciadv.abj3995

ScienceAdvances

Formation of cellular close-ended tunneling nanotubes through mechanical deformation

Minhyeok ChangO-chul LeeGayun BuJaeho OhNa-Oh YunnSung Ho RyuHyung-Bae KwonAnatoly B. KolomeiskySang-Hee ShimJunsang DohJae-Hyung JeonJong-Bong Lee

Sci. Adv., 8 (13), eabj3995. • DOI: 10.1126/sciadv.abj3995

Science Advances (ISSN) is published by the American Association for the Advancement of Science. 1200 New York Avenue NW, Washington, DC 20005. The title *Science Advances* is a registered trademark of AAAS.